THE JOURNAL OF PHYSICAL CHEMISTRY LETTERS
A JOURNAL OF THE AMERICAN CHEMICAL SOCIETY

pubs.acs.org/JPCL

Letter

Superconductivity in In_2Te_3 under Compression Induced by Electronic and Structural Phase Transitions

Jiapeng Zhen,* Wen Deng, Cong Li, Jiajia Feng, Shihui Zhang, Shun Wan, Gui Wang, Hongliang Dong, Resta A. Susilo, and Bin Chen*

Cite This: *J. Phys. Chem. Lett.* 2022, 13, 1226−1233

Read Online

ACCESS | Metrics & More | Article Recommendations

ABSTRACT: Indium telluride (In_2Te_3) is a typical layered material among III−IV families that are extremely sensitive to pressure and strain. Here, we use a combination of high-pressure electric transport, Raman, XRD, and first-principles calculations to study the electronic properties and structural evolution characteristics of In_2Te_3 under high pressure. Our results reveal the evidence of isostructure electronic transitions. First-principle calculations demonstrate that the evolution of phonon modes is associated with the transition from semiconductor to metal due to the increase in the density of states near the Fermi level. The pressure-induced metalization as a precursor monitors the structural phase transition, and then the superconductivity is produced. Further, in decompression, T_c slightly increased and remained at 3.0 GPa, and then the disorder is present and the superconductivity is suppressed. Our work not only perfects the superconducting phase of the In−Te system under pressure but also provides a reference for further superconducting research and applications.

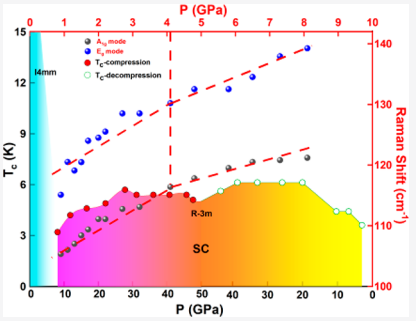

Group III2−VI3 semiconductors have drawn intense attention due to their excellent surface properties. For example, the polar α-In_2Se_3, one of the models of 2D piezoelectrics and ferroelectrics with simple crystal structures, shows its great potential in electronic and photonic applications.[1] In the case of indium telluride/selenium, people have been investigating this material since 1970 for sustainable applications in sensors, strain gauges, optoelectronic devices, radiation detectors, switching, and memory devices.[2−7] Especially, In_2Te_3 shows a higher absorption coefficient over a wide absorption range (500−2500 nm) and possesses the smallest direct bandgap of approximate value 1.1 eV in III2−VI3 compounds[8,9] whereas the monoclinic semiconductor GeAs has a bandgap of around 1 eV.[10] It also has higher radiation stability than traditional semiconductors such as Si, Ge, and GaAs.[11]

High pressure is a clean way of tuning the structure and electronic properties of materials. Related to the semiconducting compounds, one particular interest is to investigate the possible occurrence of metalization and superconductivity under pressure. Moreover, it has also been recently reported that pressure is a powerful method to drive the system into a new exotic quantum state via topological phase transition, as reported in Bi_2Se_3[12] and Sb_2Te_3.[13]

Despite the promising technological applications, few works have been reported on the behavior of III2−VI3 semiconductors such as Ga_2Te_3 and In_2Te_3 at extreme conditions, in particular high pressure. Previous studies reported the occurrence of the pressure-induced phase transition in In_2Te_3 from the ZnS-type to NaCl-type structure above 12 GPa.[14] In comparison, high-pressure studies on the isostructural In_2Se_3 led to interesting phenomena, such as pressure-induced metalization and superconductivity (SC) together with the enhancement of T_c during decompression.[15] Given the structural similarity with In_2Se_3, investigating In_2Te_3 might also lead to other interesting high-pressure properties.[15,16]

Here, we have systematically studied the pressure-dependent behavior of In_2Te_3 through Raman scattering measurement and first-principle calculations of In_2Te_3, as well as high-pressure XRD measurement up to 36.5 GPa. It can be seen from the experimental and calculated results that in the unusual Raman modes (A_{1g} and E_g), the electron−phonon coupling has a structure electronic transition of 4.1 GPa, which is related to metalization. Interestingly, we found pressure-induced SC with the phase transition in In_2Te_3 above 8 GPa with T_c = 3.2 K, T_c increases under compression reaching the maximum value of 5.7 K at 27.8 GPa, during decompression the superconductivity state could be preserved down to 3 GPa, below which it disappears.

Received: December 21, 2021
Accepted: January 26, 2022
Published: January 28, 2022

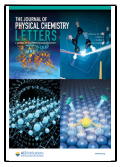

https://doi.org/10.1021/acs.jpclett.1c04124
J. Phys. Chem. Lett. 2022, 13, 1226−1233

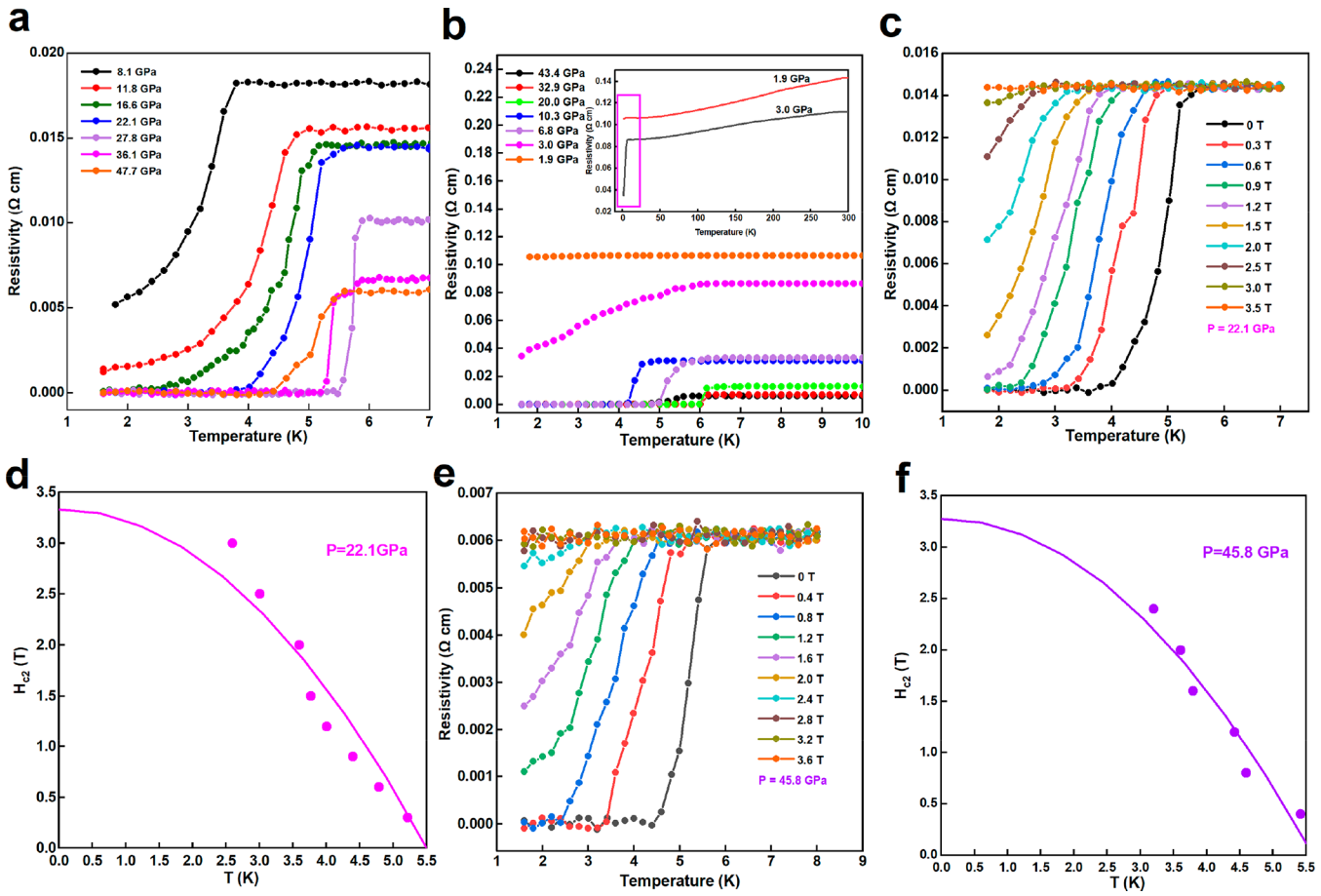

Figure 1. Temperature dependence of the resistivity of In_2Te_3 at various pressures: (a) compression; (b) decompression. The inset in (b) shows the $R-T$ curves from 1.8 to 300 K at 1.9 and 3.0 GPa. (c)−(f) Upper critical field H_{c2} and temperature dependence of the upper critical field H_{c2} of In_2Te_3 at 22.1 GPa (c, d) and 45.8 GPa (e, f). The superconducting transition of the In_2Te_3 at these pressures is given for several magnetic fields. The lines are from the GL formula to fit the data, which points to $H_{c2}(0) \approx 3.33$ and 3.28 T.

To investigate the electronic properties of In_2Te_3 under pressure, we performed high-pressure transport measurements. Figure 1a shows the temperature-dependent resistivity of In_2Te_3 at various pressures from 1.5 to 47.7 GPa. At 8.1 GPa, the resistivity shows a sudden drop at low temperature signaling the possible pressure-induced superconductivity. Indeed, zero resistivity is observed when the sample is compressed at a higher pressure of 16.6 GPa. The superconducting transition T_c is 4.3 K at 16.6 GPa, which tends to increase with increasing pressure. T_c reaches its maximum value of 5.7 K at around 27.8 GPa, above which it remains almost constant with further compression.

Pressure often has a reversible modulation effect on the semiconducting states, where the evolution of T_c during the decompression process is usually similar to the compression process. In such cases, the pressure-induced superconductivity often disappears during decompression or pressure release. In the case of In_2Te_3, we found that T_c could be preserved and slightly increases during compression. Moreover, T_c can be preserved to even as low as 3.0 GPa in the pressure release, as shown in Figure 1b. Similar behavior was also reported in the isostructural In_2Se_3;[15] however, T_c was found to disappear below 10 GPa which is higher than In_2Te_3 where the superconducting state can be preserved down to ∼3 GPa. In order to better observe the superconductivity at low pressure, we drew the $R-T$ curve over the entire temperature range under pressures of 1.9 and 3.0 GPa (as shown in Figure 1b). It can be found that there is no apparent superconductivity at 1.9 GPa. It is speculated that the superconducting behavior still exists at 3.0 GPa. Then, the reason the superconducting phenomenon becomes insignificant after below 3 GPa is due to the disorder, which inhibits superconductivity.[17]

The field dependence of resistivity at several pressure points was then measured to confirm the pressure-induced superconductivity in In_2Te_3, as shown in Figure 1c,e. As the magnetic field increases, the resistivity drop is lifted. The onset of T_c is gradually shifted to a lower temperature, and T_c is fully suppressed above 4 T. Figure 1 panels d and f depict the temperature dependence of H_{c2}. Under the limitation of the temperature range we measure, we can see the obvious linear temperature dependence of H_{c2}. By using the Ginzburg−Landau (GL) equation to fit the data, we estimated $H_c(T) = H_c(0)[1 - (T/T_c)^2] \approx 3.33$ and 3.28 T at 22.1 and 45.8 GPa. The critical fields determined using the Werthamer−Helfand−Hohenberg formula are $H_{c2}^{orb}(0) = 0.72T_c|d(H_{c2})/dT|_{T=T_c} = 3.53$ and 3.88 T,[18] which are much lower than Pauli limit field $H_p(0) = 1.84T_c = 9.02$ and 9.94 T.[19,20] This shows that the Pauli combination did not break. Recently, the similar linear temperature dependence of H_{c2} has been observed in the pressurized topological superconductor (TSC) candidate materials Bi_2Se_3 and $Cu_xBi_2Se_3$, the natural TSC candidate Au_2Pb, the noncentrosymmetric superconductor YPtBi, and

https://doi.org/10.1021/acs.jpclett.1c04124
J. Phys. Chem. Lett. 2022, 13, 1226−1233

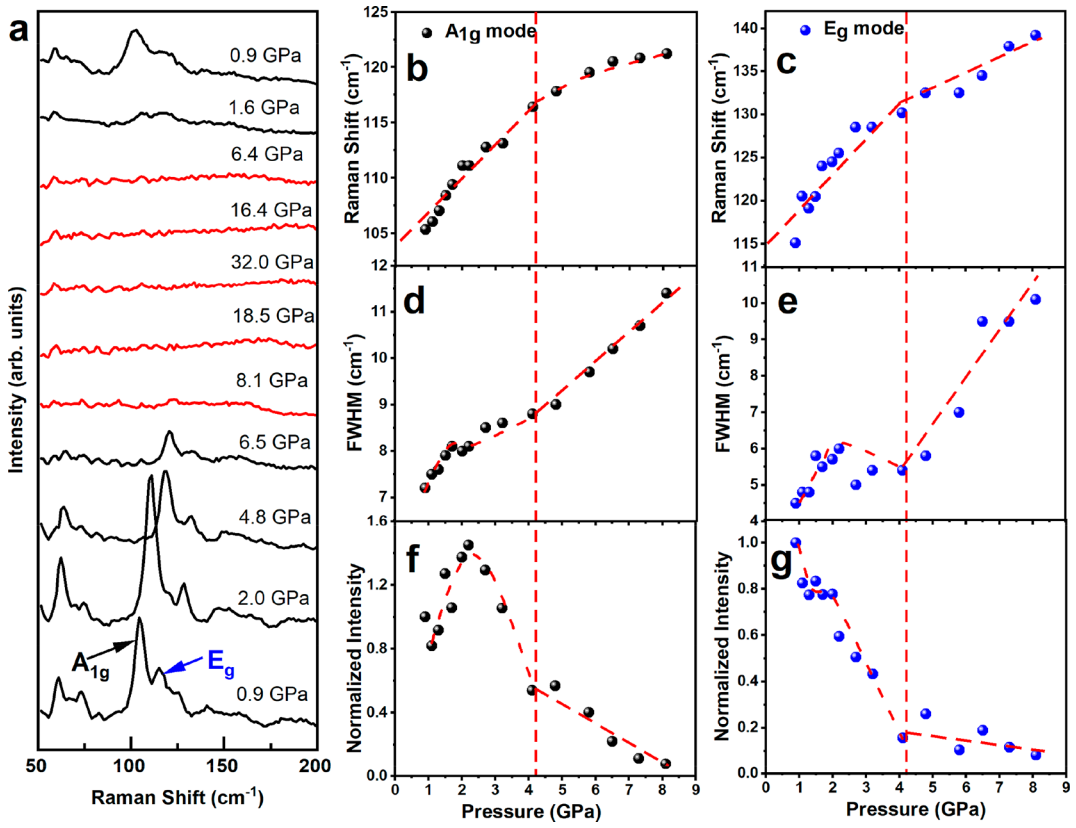

Figure 2. Raman spectra of In_2Te_3 from ambient pressure up to 32.0 GPa at room temperature (a). Pressure dependence of Raman shift of (b) A_{1g} and (c) E_g modes. FWHM of (d) A_{1g} and (e) E_g modes. The normalized intensity of (f) A_{1g} and (g) E_g modes. The red dashed lines in (a) and (b) represent the linear equation fit. The red dashed lines in (c)−(f) represent a guide to an eye. The vertical dashed line at ∼4.1 GPa represents the isostructural electronic transition in In_2Te_3.

three-dimensional topological Dirac semimetal Cd_3As_2; this is considered to be an indicator of an unconventional superconducting state under ambient pressure and high pressure.[21−25]

The Raman spectra were obtained from the powder In_2Te_3 under a 532 nm excitation laser and revealed several Raman modes between 50 and 200 cm^{-1} from 0.9 to 32.0 GPa and decompression to 0.9 GPa, as shown in Figure 2a, which is consistent with previous measurements.[26−28] In compression, all Raman peaks shift to the higher frequency, with the strongest Raman mode at about 110 cm^{-1} being first enhanced from 0.9 to 2.0 GPa, above which the intensities are then weakened from 2.7 to 8.1 GPa. According to the theoretical calculation, strong odd-order lines of the zinc-blende sublattice (111) and (311) weakened appreciably at $P > 2.7$ GPa and disappeared at 3.8 GPa, respectively. Therefore, the phase transition for In_2Te_3 may begin at $P = 2.0$ GPa, because the precision of the cubic cell determination is decreased at this pressure and it achieves the value ±0.2 Å at $P > 2.7$ GPa.[14] Since In_2Te_3 is based on defect zinc blende, the structure is the same as InTe, and the Raman mode is similar to that of InTe and shows 24 zone-center phonon modes at the Γ point:[29]

$$\Gamma = A_{1g} + 2A_{2g} + B_{1g} + 2B_{2g} + 3E_g + B_{1u} + 3A_{2u} + 4E_u$$

On the basis of the previous work,[30] the observed phonon modes at ∼105 and ∼115 cm^{-1} are assigned to A_{1g} and E_g symmetry, respectively. Lattice dynamics are very important, especially in the electronics of materials.[30−32] Therefore, it is very important to understand the behavior of the phonon modes by the influence of pressure on the electronic and topological properties. The pressure-induced phonon frequencies for A_{1g} and E_g modes are shown in Figure 2b,c. A_{1g} and E_g increase monotonically to 8.1 GPa, and the slope changes slightly at 4.1 GPa. By fitting equations for two different pressure regions (0−4.1 and 4.1−8.1 GPa), the nonlinear pressure dependence of the A_{1g} mode is analyzed; the slopes in A_{1g} and E_g mode we obtained are 3.05, 1.25 and 3.66, 1.74 cm^{-1}/GPa, respectively. The Gruneisen parameters γ are calculated by using the relation $\left(\frac{B}{\omega(P_0)} \times \frac{\partial\omega}{\partial P}\right)$, where B represents the isothermal bulk modulus (B = 17.60 GPa). So we can get the Gruneisen parameters as 0.52, 0.19 and 0.56, 0.24, and it can be observed that the pressure coefficient of the A_{1g} mode is smaller than that of the E_g mode. Due to the layer being composed of covalent bonds of Te^{2-}−In^{3+}−Te^{2-}−In^{3+} atoms, the layers are separated by the weak electrostatic interaction between the negatively charged In^{3+} and Te_4^{2-} tetrahedrons. Therefore, this is also consistent with our experimental results that the pressure coefficient of E_g mode will be greater than the A_{1g} mode.

Line width also provides important information in Raman spectroscopy, especially in relation to electronic transitions of the isostructure. The full width at half-maximum (FWHM) is inversely proportional to the phonon lifetime in the crystal system. The pressure-induced line width behaviors of the A_{1g} and E_g phonon modes are shown in Figure 2d,e. It can be

https://doi.org/10.1021/acs.jpclett.1c04124
J. Phys. Chem. Lett. 2022, 13, 1226−1233

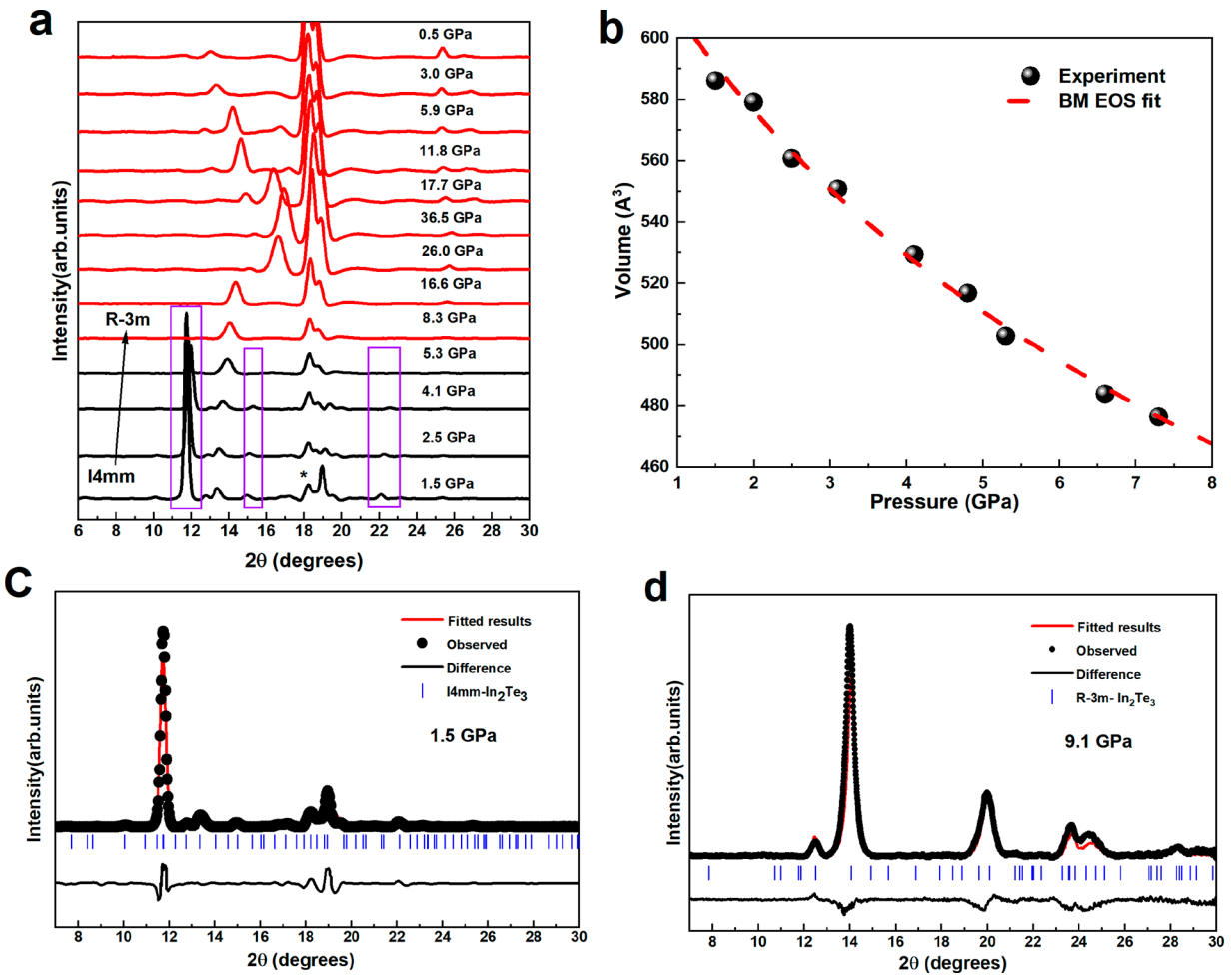

Figure 3. (a) Evolution of the X-ray diffraction (λ = 0.7160 Å) pattern with increasing and decreasing pressure. * is the Tungsten peak. There has a phase transition from *I*4*mm* to $R\bar{3}m$ at around 8.3 GPa. (b) Experimental lattice parameter volume as a function of applied hydrostatic pressure. (c, d) Rietveld refinement result of the X-ray diffraction pattern for 1.5 GPa (λ = 0.7160 Å) and 9.1 GPa (λ = 0.6199 Å). For a clearer comparison, the unified wavelength is λ = 0.7160 Å.

found that the line width of the A_{1g} and E_g modes first increases and then decreases below 4.1 GPa, and the change is relatively slow, but after this pressure is exceeded, the line width increases suddenly and rapidly. Under normal circumstances, the half-height width will increase with pressure. But the line width observed here has an abnormal behavior before 4.1 GPa, indicating that the electron−phonon coupling changes under pressure. The same phenomenon also occurs in Figure 2f,g. The intensities of A_{1g} and E_g decrease with increasing pressure, and their slopes abruptly change at 4.1 GPa. The pressure evolution results of A_{1g} and E_g are very similar, indicating that the phonon mode has a strong interaction with the electronic state modulated by a pressure exceeding 4.1 GPa. Since we found that all the Raman modes disappeared and phase transitions occurred after 8.1 GPa, we found that the abnormal phenomenon of the phonon can clearly indicate the existence of isostructure electronic transitions. This is also mutually corroborated by previous reports.[14]

To further characterize the metallic phase's crystal structure after the SC transition, the separate high-pressure powder X-ray diffraction (XRD) experiment in In_2Te_3 at 300 K was performed as shown in Figure 3a. During the compression and decompression, it is easy to see three peaks disappear apparently after 5.3 GPa (300 K, circled by quadrilaterals) to evidence the emergence of the structural transition. Through the third-order Birch−Murnaghan equation of state (BM EOS) fitting of the volume parameter, we can clearly explain its compression characteristics. The fitted parameters are B_0 = 17.6, V_0 = 648.7, and B_0' = 3.7, which can be better mutually confirmed with the previous reports.[14,29] The experimental pressure volume is fitted with the third-order BM EOS, and the formula fitting is shown in Figure 3b.[33]

$$P(V) = \frac{3B_0}{2}\left[\left(\frac{V_0}{V}\right)^{7/3} - \left(\frac{V_0}{V}\right)^{5/3}\right] \times \left\{1 + \frac{3}{4}(B_0' - 4)\left[\left(\frac{V_0}{V}\right)^{2/3} - 1\right]\right\}$$

where V_0, B_0, and B_0', respectively, represent the volume at room temperature, the isothermal body modulus, and its derivative. Next, Figure 3 panels c and d show the XRD pattern collected at 1.5 and 9.1 GPa, in which all Bragg peaks can be indexed to *I*4*mm* and $R\bar{3}m$ structures, consistent with previous reports.[34,35] So the structural phase changes affect superconductivity. In decompression, the high-pressure phase can

https://doi.org/10.1021/acs.jpclett.1c04124
J. Phys. Chem. Lett. 2022, 13, 1226−1233

also be better maintained, which also provides support for the decompression to maintain superconductivity.

On the basis of high-pressure resistivity, Raman, and XRD results, the pressure−temperature phase diagram of In_2Te_3 can be constructed as shown in Figure 4. Pressure-induced

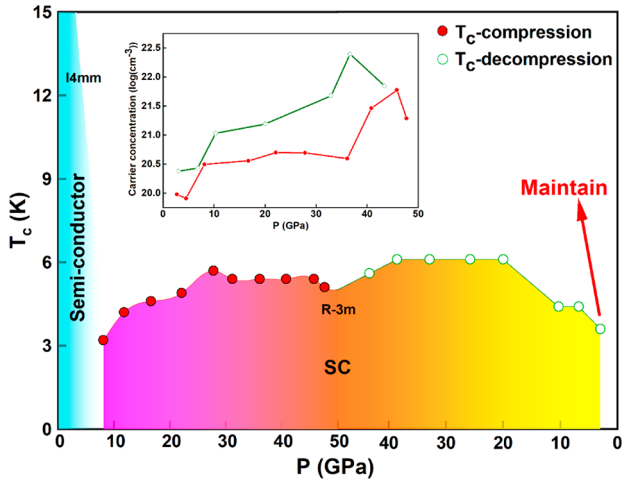

Figure 4. Phase diagram of In_2Te_3 at high pressure. The red circles represent compression; green circles represent decompression. The inset in the figure is the curve of the change of carrier concentration with pressure.

superconductivity occurs above 8 GPa. T_c slightly increases with pressure, reaching a maximum at around 28 GPa. The value of T_c remains relatively constant at higher pressure, up to ~50 GPa. On the other hand, T_c is slightly enhanced during decompression and remains relatively constant at ~6 K before decreasing during decompression below 20 GPa. T_c could be preserved down to 3 GPa but then disappears on fully releasing pressure. The superconducting state was found to occur in the $R\bar{3}m$ structure.

In order to study the electronic density of states of the Fermi surface, $N(E_F)$, and the electron−phonon coupling of In_2Te_3 in the pressure cycle, we conducted Hall effect experiments at 10 K at various pressures. As shown in Figure 4, with the increase of pressure, the carrier concentration of In_2Te_3 increased significantly at 8.1 GPa, and then the change tended to be flat until it ushered in a significant increase at 36.0 GPa. At the same time, T_c increases with pressure. During the decompression process, the carrier concentration ushered in a significant increase and then gradually decreased.

To better understand the mechanism of the superconducting phase transition more clearly, we obtained the band structure and electronic density of states of In_2Te_3 under ambient pressure, 10 GPa, and 20 GPa through first-principles calculations. We found that in the process of a pressurized superconducting transition, it has not undergone a structural phase change and has always been maintained in the *I*4*mm* phase. In_2Te_3 exhibits semiconductor characteristics under ambient pressure, with a bandgap of approximately 0.22 eV, and then it transforms into metal as the pressure increases. In order to obtain the mechanism of superconductivity after pressurization, we compared the electronic band structure and projected electronic density of states (DOS) at ambient pressure and at 9 GPa, as shown in Figure 5. Several bands passing through the Fermi level confirmed the semiconductor state and metallic properties of these two states. The electronic densities of states of the two states have significant similarity.

According to the BCS and Mcmillan−Allen−Dynes theory,[36,37] when the electron−phonon coupling (λ) is strong enough to overcome the Coulomb repulsion (μ), the electrons form a "Cooper pair", leading to the emergence of superconductivity. Coulomb repulsion is not material-sensitive,[38] but the electron−phonon coupling may vary with the material or structure as

$$\lambda = N(E_F)D^2/M\omega_{ph}^2$$

$$T_c = \frac{\Theta}{1.2}\exp[-1.04(1+\lambda)/(P\lambda - \mu^*(1+0.62\lambda))]$$

where $N(E_F)$ is the electron density of state at the Fermi level, D is the deformation potential, M and ω_{ph} are the effective atomic mass and phonon frequency, μ^* is using 0.1, and Debye Θ is used for the characteristic phonon frequency. respectively. An increase in the electron density of states on the Fermi surface usually enhances electron−phonon coupling, thereby enhancing T_c. In contrast, stress-induced phonon enhancement can suppress T_c, such as in the case of MgB_2.[39] In In_2Te_3, from 8.1 to 27.8 GPa, a slight enhancement of T_c is accompanied by the increasing carrier concentration in the compression, indicating their correlation. When it is further compressed above 27.8 GPa, the carrier concentration increases significantly, and other factors such as phonon stiffening have an impact on the evolution of T_c. It seems that these two opposite mechanisms (carrier concentration and phonon intensity) determine the change of T_c in pressurized In_2Te_3.

Our results indicate that the In_2Te_3 shows the maximum T_c above 5.7 K at 27.8 GPa, which is the highest transition temperature in this type of material. It is well-known that the phase diagrams of In_2Te_3 and Ga_2Te_3 sesquitellurides are almost identical, except that the $\alpha \rightarrow \beta$ transition of In_2Te_3 occurs at lower pressure.[14,34,35] However, besides a similar phase transition sequence, we observed pressure-induced superconductivity above 8 GPa, which has never been reported previously and thus could enrich the high-pressure phase diagram of the In−Te system.[40] Compared with results for other isostructural compounds, the superconductivity in In_2Te_3 appears at a higher pressure. For example, in Bi_2Te_3, the superconductivity occurs without structural phase transition T_c of 3 K between 3 and 6 GPa.[13] Another isostructural compound Sb_2Te_3 becomes superconductivity with $T_c \sim 6$ K at around 7.6 GPa.[41]

In summary, we have explored the lattice dynamics and superconductivity of In_2Te_3 under 50 GPa compression. Our Raman spectroscopy experiment revealed the pressure-induced structural transformation of In_2Te_3, which is consistent with the XRD experiments. Further, at a relatively low pressure of 4.1 GPa, an isostructure electronic transition can be seen from the anomaly of the FWHM of the phonon mode (A_{1g} and E_g). DFT calculations show that the observed anomaly is related to the pressure-induced metalization near 4.1 GPa. With the phase transition, In_2Te_3 produces superconductivity and the maximum T_c is up to 5.7 K, which is the highest T_c reported in this type of material at lower pressures. More interestingly, during the decompression process, T_c increases and the superconductivity remains within 3.0 GPa. Our results limit the high-pressure phase diagram and superconductivity of this binary In_2Te_3 material. More importantly, we also observed an increase in pressure-induced superconductivity, further dem-

https://doi.org/10.1021/acs.jpclett.1c04124
J. Phys. Chem. Lett. 2022, 13, 1226−1233

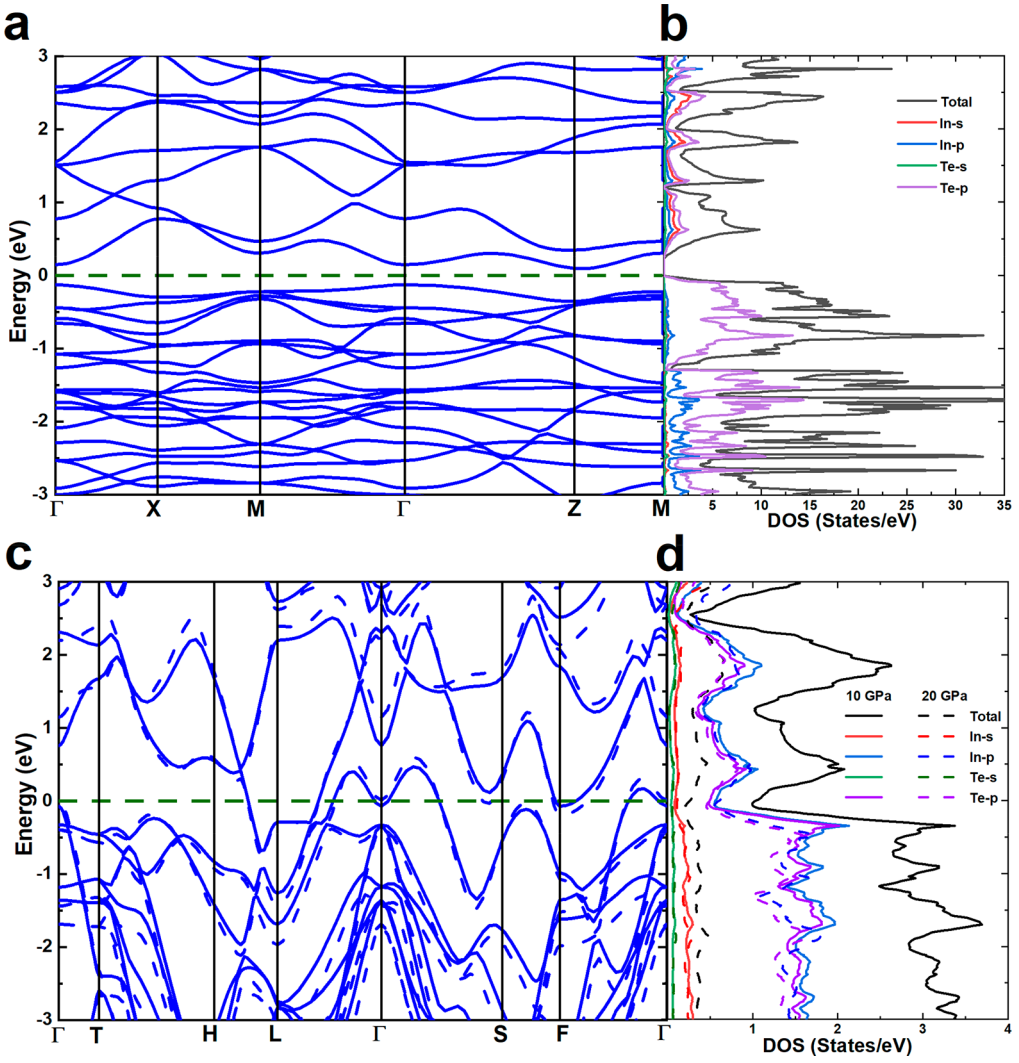

Figure 5. Band structure of the tetragonal phase *I*4*mm* (a) and $R\bar{3}m$ (c). Calculated density of electronic states at ambient pressure (b) and at 10 GPa and 20 GPa (d), where black represents the total, red and blue represent the s and p orbit of the In atom, and green and purple represent the s and p orbit of the Te atom. The common vertical axis (energy) is used to more intuitively show the relationship between the energy band structure and the electronic density of states, and the horizontal axis represents the path point and the density of states.

onstrating the possibility of maintaining pressure-induced superconductivity at lower or even higher T_c environmental pressures. This material can maintain a higher electron−phonon coupling carrier concentration under lower reduced pressure and can also exhibit a significantly reduced pressure-induced superconductivity enhancement. This research provides the possibility to explore the practical application of pressure-induced superconductors.

EXPERIMENT METHODS

Sample Preparation and Characterization at Ambient Pressure. Sample Preparation and Characterization. The high-purity samples of In_2Te_3 were brought from Aladdin (https://www.aladdin-e.com). The α-In_2Te_3 sample was characterized by PANalytical Empyrean X-ray diffraction with a wavelength of 1.5406 Å. Powder diffraction patterns were well-indexed using the previously reported crystal structural data.[14]

Pressure-Dependent Electrical Transport Measurements. The van der Pauw conductivity method was used to research the electron transport characteristics of the CuBe alloy symmetrical diamond anvil (DAC) at high pressure and low temperature. The pressure was generated by a pair of diamonds with a diameter of 300 μm. The gasket made of CuBe was pressed tightly, and a hole with the diameter of a diamond drill was drilled in the center of the gasket. The cubic boron nitride (cBN) epoxy insulating layer was prepared to protect the electrode leads from the metal gasket. Finally, a hole with a diameter of 120 μm was drilled in the center of the c-BN gasket. Silicone oil was used as the pressure transmission medium. Four platinum bars were in contact with the sample in the cavity. The temperature-dependent resistivity was obtained from the warming up progress in a homemade multifunctional measurement system (1.8−300 K, 0−9 T, Cryomagnetics Inc.).

Pressure-Dependent Raman Spectroscopic Measurements. A micro-Raman system (Renishaw, UK) with a 532 nm laser excitation was applied to obtain the sample's Raman spectra. The DAC had a pair of 300 μm diamonds with a 300 μm culet size with a T301 steel gasket. Silicone oil was used as a pressure transmission medium.

Pressure-Dependent Structural Characterization. High-pressure X-ray powder diffraction measurements were

https://doi.org/10.1021/acs.jpclett.1c04124
J. Phys. Chem. Lett. 2022, 13, 1226−1233

carried out on GTS up to 36 GPa at room temperature using the Bruker D8 Quest diffractometer equipped with Mo Kα (λ = 0.7160 Å) radiation for most data. For some data, the synchrotron radiation X-ray diffraction (SR-XRD) experiments with a wavelength of 0.6199 Å were performed at beamline 15U1, Shanghai Synchrotron Radiation Facility (SSRF), China. Data were collected with an Sb-type cell with an X-ray window opening of 20°. The data refinements were conducted with the program GSAS. Powder diffraction patterns were well-indexed using the previously reported crystal structural data.[14,29]

Density Functional Theory Calculations. All the density functional theory (DFT) computations were conducted by adopting the Vienna Ab initio Simulation Package (VASP).[42] The interactions of ion-electron were depicted using the projector augmented wave approach,[43,44] and the general gradient approximation in the Perdew−Burke−Ernzerhof (PBE)[45] form was applied. The convergence criteria were set to 0.001 eV $Å^{-1}$ and 10^{-8} eV for the residual force and energy during structure relaxation. The plane-wave cutoff energy was set as 400 eV, and 2 × 2 × 2 k-points served as samples of the Brillouin region.[46]

AUTHOR INFORMATION

Corresponding Authors

Jiapeng Zhen − *Center for High Pressure Science and Technology Advanced Research, Beijing 100094, People's Republic of China;* orcid.org/0000-0002-5321-6337; Email: jiapeng.zhen@hpstar.ac.cn

Bin Chen − *Center for High Pressure Science and Technology Advanced Research, Beijing 100094, People's Republic of China*; Email: chenbin@hpstar.ac.cn

Authors

Wen Deng − *Center for High Pressure Science and Technology Advanced Research, Beijing 100094, People's Republic of China*

Cong Li − *Center for High Pressure Science and Technology Advanced Research, Beijing 100094, People's Republic of China*

Jiajia Feng − *Center for High Pressure Science and Technology Advanced Research, Beijing 100094, People's Republic of China*

Shihui Zhang − *Center for High Pressure Science and Technology Advanced Research, Beijing 100094, People's Republic of China*

Shun Wan − *Center for High Pressure Science and Technology Advanced Research, Beijing 100094, People's Republic of China*

Gui Wang − *Center for High Pressure Science and Technology Advanced Research, Beijing 100094, People's Republic of China*

Hongliang Dong − *Center for High Pressure Science and Technology Advanced Research, Beijing 100094, People's Republic of China*

Resta A. Susilo − *Center for High Pressure Science and Technology Advanced Research, Beijing 100094, People's Republic of China;* orcid.org/0000-0003-0799-7416

Complete contact information is available at: https://pubs.acs.org/10.1021/acs.jpclett.1c04124

Notes

The authors declare no competing financial interest.

ACKNOWLEDGMENTS

The authors thank Dr. Resta Agung Susilo for helpful discussions. This work was supported by the National Natural Science Foundation of China (NSFC) under grant number U1530402. Theoretical work was carried out at the Beijing Super Cloud Computing Center of China. We thank beamline BL15U1 at the Shanghai Synchrotron Radiation Facility. The electric transport, Raman spectroscopy, and most XRD measurements were performed at the Center for High-Pressure Science and Technology Advanced Research.

REFERENCES

(1) Yu, Z.; Di, W.; Zhu, Y.; Cho, Y.; Lai, K. Out-of-Plane Piezoelectricity and Ferroelectricity in Layered α-In_2Se_3 Nanoflakes. *Nano Lett.* **2017**, *17*, 5508−5513.

(2) Yang, X.; Banerjee, A.; Xu, Z.; Wang, Z.; Ahuja, R. Interfacial aspect of ZnTe/In_2Te_3 hetero-structures as an efficient catalyst for the hydrogen evolution reaction. *J. Mater. Chem. A* **2019**, *7*, 27441−27449.

(3) Desai, R. R.; Lakshminarayana, D.; Patel, P. B.; Panchal, C. J. Indium sesquitelluride (In_2Te_3) thin film strain gauge. *Sens. Actuators, A* **2005**, *121*, 405−409.

(4) Safdar, M.; Wang, Z.; Mirza, M.; Butt, F. K.; Wang, Y.; Sun, L.; He, J. Telluride-based nanorods and nanosheets: synthesis, evolution and properties. *J. Mater. Chem. A* **2013**, *1*, 1427−1432.

(5) Sun, H.; Lu, X.; Chi, H.; Morelli, D. T.; Uher, C. Highly efficient $(In_2Te_3)_x(GeTe)_{3-3x}$ thermoelectric materials: a substitute for TAGS. *Phys. Chem. Chem. Phys.* **2014**, *16*, 15570−15575.

(6) Sathyamoorthy, R.; Matheswaran, P.; Asokan, K. Synthesis of α-In_2Te_3 thin films from In/Te bilayer by Si ion irradiation. *Radiat. Eff. Defects Solids* **2012**, *167*, 799−806.

(7) Wang, J.; Jin, F.; Cao, X.; Cheng, S.; Liu, C.; Yuan, Y.; Fang, J.; Zhao, H.; Li, J. In_2Te_3 thin films: a promising nonlinear optical material with tunable nonlinear absorption response. *RSC Adv.* **2016**, *6*, 103357−103363.

(8) Lee, J.-H.; Park, B.-O. Transparent conducting ZnO:Al, In and Sn thin films deposited by the sol-gel method. *Thin Solid Films* **2003**, *426*, 94−99.

(9) Perananthan, P.; Jeyachandran, Y. L.; Viswanathan, C.; Praveena, N. N.; Chitra, P. C.; Mangalaraj, D.; Narayandass, Sa.K. The effect of annealing on vacuum-evaporated copper selenide and indium telluride thin films. *Mater. Charact.* **2007**, *58*, 756−764.

(10) Rau, J. W.; Kannewurf, C. R. Optical Absorption, Reflectivity, and Electrical Conductivity in GeAs and $GeAs_2$. *Phys. Rev. B* **1971**, *3*, 2581−2587.

(11) Volovichev, I.N.; Gurevichb, Y. G.; Koshkinb, V.M. Reliable rectifiers and photovoltaic converters for high levels of ionizing irradiation. *Microelectron. J.* **1998**, *29*, 535−542.

(12) Hor, Y. S.; Williams, A. J.; Checkelsky, J. G.; Roushan, P.; Seo, J.; Xu, Q.; Zandbergen, H. W.; Yazdani, A.; Ong, N. P.; Cava, R. J. Superconductivity in $Cu_xBi_2Se_3$ and its Implications for Pairing in the Undoped Topological Insulator. *Phys. Rev. Lett.* **2010**, *104*, 057001.

(13) Zhu, J.; Zhang, J. L.; Kong, P. P.; Zhang, S. J.; Yu, X. H.; Zhu, J. L.; Liu, Q. Q.; Li, X.; Yu, R. C.; Ahuja, R.; et al. Superconductivity in Topological Insulator Sb_2Te_3 Induced by Pressure. *Sci. Rep.* **2013**, *3* (5), 2016.

(14) Serebryanaya, N. R. The Crystal Structure of Pressure-Induced Phases of In_2Te_3 and Ga_2Te_3. *Powder Diffraction* **1992**, *7*, 99−102.

(15) Ke, F.; Dong, H.; Chen, Y.; Zhang, J.; Liu, C.; Zhang, J.; Gan, Y.; Han, Y.; Chen, Z.; Gao, C. Decompression-Driven Superconductivity Enhancement in In_2Se_3. *Adv. Mater.* **2017**, *29*, 1701983.

(16) Shchennikov, V. V.; Savchenko, K. V.; Popova, S. V. Electrical properties of the high-pressure phases of gallium and indium tellurides. *Phys. Solid State* **2000**, *42*, 1036−1040.

(17) Bose, D.; Sen, S.; Joshi, D.; Vaidya, S. Resistivity studies on Ga_2Te_3 and In_2Te_3 under high pressures. *Mater. Lett.* **1982**, *1* (2), 61−63.

(18) Werthamer, N. R.; Helfand, E.; Hohenberg, P. C. Temperature and Purity Dependence of the Superconducting Critical Field, H_{c2}.III. Electron Spin and Spin-Orbit Effects. *Phys. Rev.* **1966**, *147*, 295−302.
(19) Clogston, A. M. Upper Limit for the Critical Field in Hard Superconductors. *Phys. Rev. Lett.* **1962**, *9*, 266−267.
(20) Chandrasekhar, B. S. A note on the maximum critical field of high-field superconductors. *Appl. Phys. Lett.* **1962**, *1*, 7−8.
(21) Kirshenbaum, K. P.; Syers, S.; Hope, A. P.; Butch, N. P.; Jeffries, J. R.; Weir, S. T.; Hamlin, J. J.; Maple, M. B.; Vohra, Y. K.; Paglione, J. Pressure-Induced Unconventional Superconducting Phase in the Topological Insulator Bi_2Se_3. *Phys. Rev. Lett.* **2013**, *111*, 087001−087005.
(22) Bay, T. V.; et al. Superconductivity in the Doped Topological Insulator $Cu_xBi_2Se_3$ under High Pressure. *Phys. Rev. Lett.* **2012**, *108*, 057001.
(23) Xing, Y.; et al. Superconductivity in topologically nontrivial material Au_2Pb. *Npj Quant. Mater.* **2016**, *1*, 16005.
(24) Bay, T. V.; Naka, T.; Huang, Y. K.; de Visser, A. Superconductivity in noncentrosymmetric YPtBi under pressure. *Phys. Rev. B* **2012**, *86*, 064515.
(25) He, L.; Jia, Y.; Zhang, S.; Hong, X.; Jin, C.; Li, S. Pressure-induced superconductivity in the three-dimensional topological Dirac semimetal Cd_3As_2. *Quantum Materials* **2016**, *1*, 16014.
(26) Finkman, E.; Tauc, J.; Kershaw, R.; Wold, A. A. Lattice dynamics of tetrahedrally bonded semiconductors containing ordered vacant sites. *Phys. Rev. B* **1975**, *11* (10), 3785−3789.
(27) Emziane, M.; Bernede, J.; Ouerfelli, J.; Essaidi, H.; Barreau, A. J. M. C. A novel method for preparing α-In_2Te_3 polycrystalline thin films. *Mater. Chem. Phys.* **1999**, *61* (3), 229−236.
(28) Zhang, S.; Zhang, J.; Liu, B.; Jia, X.; Wang, G.; Chang, H. J. S. R. Large area growth of few-layer In_2Te_3 films by chemical vapor deposition and its magnetoresistance properties. *Sci. Rep.* **2019**, *9*, 10951.
(29) Woolley, J. C.; Pamplin, B. R.; Holmes, P. J. The ordered crystal structure of In_2Te_3. *J. Less-Common Met.* **1959**, *1*, 362−376.
(30) Rajaji, V.; Dutta, U.; Sreeparvathy, P. C.; Sarma, S. C.; Sorb, Y. A.; Joseph, B.; Sahoo, S.; Peter, S. C.; Kanchana, V.; Narayana, C. Structural, vibrational, and electrical properties of 1T-$TiTe_2$ under hydrostatic pressure: Experiments and theory. *Phys. Rev. B* **2018**, *97*, 085107−085119.
(31) Nizametdinova, M. A. Raman Spectrum of InTe and TlSe Single Crystals. *Phys. Status Solidi B* **1980**, *97*, K9.
(32) Bera, A.; Pal, K.; Muthu, D. V. S.; Sen, S.; Guptasarma, P.; Waghmare, U. V.; Sood, A. K. Sharp Raman Anomalies and Broken Adiabaticity at a Pressure Induced Transition from Band to Topological Insulator in Sb_2Se_3. *Phys. Rev. Lett.* **2013**, *110*, 107401−107411.
(33) Murnaghan, F. D. The Compressibility of Media under Extreme Pressures. *Proc. Natl. Acad. Sci. U.S.A.* **1944**, *30*, 244−247.
(34) Ke, F.; Liu, C.; Gao, Y.; Zhang, J.; Tan, D.; Han, Y.; Ma, Y.; Shu, J.; Yang, W.; Chen, B.; Mao, H.-K.; Chen, X.-J.; Gao, C.; et al. Interlayer-glide-driven isosymmetric phase transition in compressed In_2Se_3. *Appl. Phys. Lett.* **2014**, *104*, 212102.
(35) Rasmussen, A. M.; Teklemichael, S. T.; Mafi, E.; Gu, Y.; McCluskey, M. D. Pressure-induced phase transformation of In_2Se_3. *Appl. Phys. Lett.* **2013**, *102*, 062105.
(36) Tamura, K.; Misonou, M.; Endo, H. Electrical Resistivity of Liquid Te, Ga_2Te_3, In_2Te_3 and Tl_2Te under High Pressure. *J. Phys. Soc. Jpn.* **1979**, *46*, 637−642.
(37) McMillan, W. L. Transition Temperature of Strong-Coupled Superconductors. *Phys. Rev.* **1968**, *167*, 331−336.
(38) Si, C.; Liu, Z.; Duan, W. H.; Liu, F. First-Principles Calculations on the Effect of Doping and Biaxial Tensile Strain on Electron-Phonon Coupling in Graphene. *Phys. Rev. Lett.* **2013**, *111*, 196802−196806.
(39) Tomita, T.; Hamlin, J. J.; Schilling, J. S.; Hinks, D. G.; Jorgensen, J. D. Dependence of Tc on hydrostatic pressure in superconducting MgB_2. *Phys. Rev. B* **2001**, *64*, 092505.
(40) Geller, S.; Jayaraman, A.; Hull, G. W., Jr Crystal chemistry and superconductivity of pressure-induced phases in the In-Te system. *J. Phys. Chem. Solids.* **1965**, *26*, 353−361.
(41) Zhang, J. L.; Zhang, S. J.; Weng, H. M.; Zhang, W.; Yang, L. X.; Liu, Q. Q.; Feng, S. M.; Wang, X. C.; Yu, R. C.; Cao, L. Z.; et al. Pressure-induced superconductivity in topological parent compound Bi_2Te_3. *Proc. Natl. Acad. Sci. U.S.A.* **2011**, *108*, 24−28.
(42) Kresse, G.; Furthmüller, J. Efficient iterative schemes for ab initio total-energy calculations using a plane-wave basis set. *Phys. Rev. B* **1996**, *54*, 11169−11174.
(43) Blöchl, P. E. Projector augmented-wave method. *Phys. Rev. B* **1994**, *50*, 17953−17957.
(44) Kresse, G.; Joubert, D. From ultrasoft pseudopotentials to the projector augmented-wave method. *Phys. Rev. B* **1999**, *59*, 1758−1762.
(45) Perdew, J. P.; Burke, K.; Ernzerhof, M. Generalized Gradient Approximation Made Simple. *Phys. Rev. Lett.* **1996**, *77*, 3865−3868.
(46) Monkhorst, H. J.; Pack, J. D. Special points for Brillouin-zone integrations. *Phys. Rev. B* **1976**, *13*, 5188−5192.

https://doi.org/10.1021/acs.jpclett.1c04124
J. Phys. Chem. Lett. 2022, 13, 1226−1233